Radar Observations and Simulation of the Melting Layer of Precipitation

Klaassen, Wim

Published in:
Journal of the Atmospheric Sciences

DOI:
10.1175/1520-0469(1988)045<3741:ROASOT>2.0.CO;2

Publication date:
1988

Radar Observations and Simulation of the Melting Layer of Precipitation

WIM KLAASSEN

Faculty of Electrical Engineering, Delft University of Technology, The Netherlands

(Manuscript received 22 June 1987, in final form 2 February 1988)

ABSTRACT

The melting layer in precipitation is physically modeled and compared with high resolution Doppler radar data. The model includes a new formulation of the dielectric properties and can handle all ice particles with densities ranging from pure snow to hail. The air temperature is calculated from the vertical air velocity. The model can simulate the aggregation and breakup of the melting particles.

The melting layer is often observed as a bright band; the prominence of the bright band is related to the density of particles before melting. The width of the band increases with the rain intensity; according to the model this is mainly caused by an increase in the almost isothermal layer at the upper part of the melting layer.

The results of the model are in good agreement with Doppler radar observations. According to the model, the reflectivity is very sensitive to the dielectric properties and density of the melting particles and the influence of aggregation is restricted. Because of the assumption of stationarity the best results are found in stratiform precipitation.

1. Introduction

This study is set up primarily to calculate the attenuation of radio waves in the melting layer, since present models (Nishitsuji et al. 1983; Leitao and Watson 1986) have a limited physical basis. An additional reason to study the melting layer is found in the withdrawal of melting heat from the atmosphere (Wexler et al. 1954), that may result in downdrafts (Atlas et al. 1969). Finally, the increased reflectivity in the melting layer or bright band may cause errors in the radar-derived rain intensity predictions (Smith 1986).

The causes for high reflectivity in the bright band are reviewed by Battan (1973): A reflectivity excess of some 5 dB, compared with the underlying rain can be explained by the increase of the dielectric constant, followed by an increase of the fall velocity of the melting snowflakes. Higher reflectivities are common in the bright band. Two types of explanations are found in the literature for these reflectivities: Aggregation and breakup (Austin and Bemis 1950; Lhermitte and Atlas 1963) and a distribution of the melted water as a shell around the flake (Aden and Kerker 1951; Dissanayake and McEwan 1978).

Although Ohtake (1969) suggests that aggregation and breakup of melting particles can be disregarded, recent observations with filter paper on a mountain slope (Yokoyama et al. 1985), with an optical spectrometer in aircraft (Stewart et al. 1984) and with a two-wavelength radar (Yokoyama et al. 1984), show the significance of aggregation and breakup. However, the observed amount seems insufficient for explanation of the high reflectivity in the bright band. The assumption that the melted water forms a shell around the particle may hold for hail (Rasmussen et al. 1984), but for snow the melted water lodges inside (Knight 1979; Matsuo and Sasyo 1981a; Fujiyoshi 1986) due to surface tension considerations. A study of the effective dielectric constant of melting snow by Battan and Bohren (1982) motivated the effort to model realistically the reflectivity.

In setting up a simulation model, we have to face the problem of the transient nature of the bright band. The bright band is mainly observed in stratiform precipitation, but even there it may disappear suddenly. To include this feature we have varied the density of the ice particles from pure snow to graupel and hail. To find a realistic aggregation rate of the ice particles (Passarelli and Srivastava 1979; Sasyo and Matsuo 1985) the density is scattered around the mean value.

The width of the bright band is underestimated in the case where the melting rate is calculated from the wet adiabatic lapse rate. An improvement is obtained by including an almost isothermal air temperature layer at the top of the melting layer. Such a layer is calculated from the energy balance of the rising air with a simple correction for the melting heat released.

As the Doppler radar observations are taken in a fixed vertical position, a one-dimensional model is chosen. With this assumption it is possible to include many microphysical phenomena in the model by keeping the computation time acceptable. The reflec-

Corresponding author address: Dr. Wim Klaassen, Telecommunications Systems Group 20-28, Dept. of Electrical Engineering, P.O. Box 5031, 2600 GA Delft, The Netherlands.

tivity is calculated by assuming spherical particles and the vertical air velocity is assumed constant in the melting layer.

The calculations start from the height with 0°C wet-bulb air temperature. In small height downward steps the melted fraction, air temperature, particle size distribution, fall velocity and radar reflectivity are calculated until the particles have melted. Five parameters are extracted from the radar observations of the melting layer; four are used to fit the input data of the model and the other is used for verification.

2. The model of the melting layer

a. The melted fraction

The melted fraction f of an ice particle is obtained by integration from the melting rate df/dt, given by

$$mL_f df/dt = 2\pi d_f F C_h (k\Delta T + KL_v \Delta\rho_v), \quad (1)$$

where

- m the mass of the particle $m = \pi/6\rho_f d_f^3$,
- L_f the latent heat of fusion of water; $L_f = 335$ J g^{-1},
- L_v the latent heat of condensation of water; $L_v = 2500$ J g^{-1},
- d_f the diameter of the melting particle, given in section 2c,
- ρ_f the density of the melting particle, section 2d,
- F the ventilation factor of spherical particles, dependent, on the Reynolds number and increasing from 1 for the smallest particles to ≈ 10 for the largest, and
- C_h an empirical correction factor for nonspherical particles, section 2f,
- ΔT the temperature difference between the melting particle and the surrounding air, section 2b,
- $\Delta\rho_v$ the water vapor density difference between the saturated value at the melting particle and the surrounded air, section 2b,

$$k = 0.024 \text{ J/(m s K)}$$

$$K = 225.10^{-6} \text{ m}^2 \text{ s}^{-1}.$$

Equation (1) is integrated from the 0°C height downward. The time dependence is converted to a height dependence using:

$$df/dt = (df/dz)(dz/dt) = df/dz/V_d, \quad (2)$$

where z is the height, V_d the Doppler fall velocity of the particle, $V_d = V - V_a$, V the fall velocity, related to the surrounding air, section 2d, and V_a the vertical air velocity, taken as fitting parameter.

In the model, downward fall- and upward air-velocities are taken positive to get positive values as a rule. With high upward air velocities V_d may become negative at the first height interval for some particles. In that case it is assumed that the particle has already melted at the first height. When the Doppler fall velocity of the melted particle is negative as well, the drop will be blown to heights above the 0°C height.

b. Air temperature and humidity

The vertical air temperature gradient is calculated from the wet adiabatic lapse rate with a correction for the released melting heat:

$$(C_p dT + L_v dr_s - RTdp/p)|V_a| + V_d H_f = 0, \quad (3)$$

where C_p is the specific heat of the air at constant pressure, r_s the saturated mixing ratio of water in the air, R the gas constant; $R = 287$ J kg^{-1} K^{-1}, p the air pressure, and H_f the fusion heat, released by the air.

Equations (1) and (3) are a coupled pair implying a negative feedback: a high air temperature increases the melting rate resulting in a decrease of the air temperature. A good stability is found with a height step of 10 m. During the first height steps an almost isothermal layer is found when all particles melt. As the melting process continues, an increasing number of particles will have already melted so that there are fewer melting particles remaining. Consequently, less melting heat is absorbed and the lapse rate approaches the wet adiabatic one. The height of the almost isothermal layer is proportional to the precipitation intensity and inversely proportional to the vertical air velocity. An increase of the 0°C layer with increasing rain intensity was observed by Matsuo (1984). The dependence on vertical air velocity can be understood intuitively: without supply of new air the air would continue to cool down because of the release of melting heat. With rising air the release of melting heat would result in an unstable lapse rate. The instability is eliminated by taking the absolute value of the vertical air velocity; this implies that the cooled air is transported downwards. A minimum velocity of 0.05 m s^{-1} is assumed in order to prevent an unrealistically large isothermal layer. Equation (3) is used to calculate the equilibrium situation; however, it should be noted that the air temperature only slowly approaches equilibrium (Atlas et al. 1969).

The air is assumed to be saturated with water. In convective clouds this is a coarse approximation, but Matsuo and Sasyo (1981b) found that the melting rate is hardly affected by the humidity of the air when melting is calculated from the wet-bulb temperature.

c. Particle size distribution

The model starts with a gamma distribution of particle sizes:

$$N(d_w) = N_0 d_w^2 \exp(-5.67 d_w/d_0), \quad (4)$$

where N is the particle number density (mm^{-1} m^{-3}), d_w the particle size, expressed as diameter after melting or melted diameter (mm), N_0 the particle number density constant, and d_0 the median particle size (mm).

The particle size distribution may change during melting because of 1) variations in fall velocity, 2) condensation of water vapor on the melting particles, and 3) aggregation and breakup. The consequences of these effects are as follows:

1) In the stationary situation the requirement of mass conservation results in an equal inflow and outflow of particles in a certain air volume, giving a number density inversely proportional to the fall velocity:

$$N(d)V(d) = \text{const.} \tag{5}$$

Equation (5) gives a first reason for the existence of the bright band: the reflectivity is proportional to the particle number density and thus inversely proportional to the fall velocity. Due to melting, the fall velocity in stratiform precipitation increases from 2 to 6 m s^{-1} (Lhermitte and Atlas 1963), resulting in a decrease in reflectivity of some 5 dB.

2) The melting heat is received from sensible heat (the particle is colder than the surrounding air) and latent heat (the saturated water vapor pressure on the cold particle is smaller than the water vapor pressure of the surrounding air). Due to latent heat flux the melted diameter of the particle grows during melting. As the model does not simulate the transport of water vapor, the air is assumed to be saturated with water. This results in an increase of about 10% in water mass during melting.

3) Aggregation is caused by the collision of particles of different fall speeds. The impact of the collision may result in the breakup of a particle. This is called collisional breakup. Breakup may occur as well when the particle becomes unstable, for instance, because of melting. This is called spontaneous breakup. We will discuss these phenomena next.

The collision between two particles will result in one particle of the combined mass (aggregation) or a large number of smaller particles (breakup). We use the criterion of List and Gillespie (1976), who find breakup when the smallest drop exceeds 1 mm. For melting particles we assume breakup when the amount of water in the smallest particle exceeds the amount of water in a 1 mm drop. According to Brazier-Smith et al. (1973), an average of three satellite drops is formed per breakup. The mass distribution per fragment is given as 1.6%, 11.4% and 87%.

The chance of spontaneous breakup is negligible for hail that has a diameter below 9 mm (Rasmussen et al. 1984). According to Fujiyoshi (1986) spontaneous breakup is observed frequently during the melting of snow, and the largest breakup fragments are found in the final stage of melting. From these qualitative findings, the model optionally includes spontaneous breakup for all particles with initial density below 0.2 g cm^{-3} when 80% of the mass is melted with a fragment distribution equal to that given for collisional breakup.

To conserve mass, the number density of the particles that result from aggregation and breakup is corrected for deviations in fall velocity between the initial and the resulting particles.

d. Density of the particles

The density of the melting particles affects the chance for collisions between particles (through their cross section), the fall velocity and the reflectivity. The density of snow is given by Magano and Nakamura (1965) as a function of size, but this relation is composed of measurements of dry as well as of wet (partly melted) snowflakes. For dry flakes only, the measurements can be represented more accurately by

$$\tilde{\rho} = 0.7/d_w \tag{6}$$

where $\tilde{\rho}$ is the mean density in g cm^{-3}. The measurements on snow density by Magano and Nakamura (1965) and Hobbs et al. (1974) both show a large scatter that seems to be realistic. The scatter has a considerable influence on the fall velocity and collision efficiency of the flakes. The scatter is represented by

$$\rho_s = \tilde{\rho} \exp G \tag{7}$$

where ρ_s is the actual snow density and G is a random variable with a Gaussian distribution with a zero mean and unity standard deviation. To eliminate unrealistic values the density is truncated at 0.005 and 0.9 g cm^{-3}, the latter representing the density of pure ice ρ_i. The density is calculated for melted drop size classes of 0.05 mm wide between 0 and 5 mm (Fig. 1).

Equations (6–7) represent the density of dry aggregated snow. Other ice particles are likely to have a density ρ_e between that of dry snow and pure ice, or

$$\rho_e = \rho_s^{1-e} \rho_i^{e}, \tag{8}$$

where e is an empirical density factor, ranging from 0

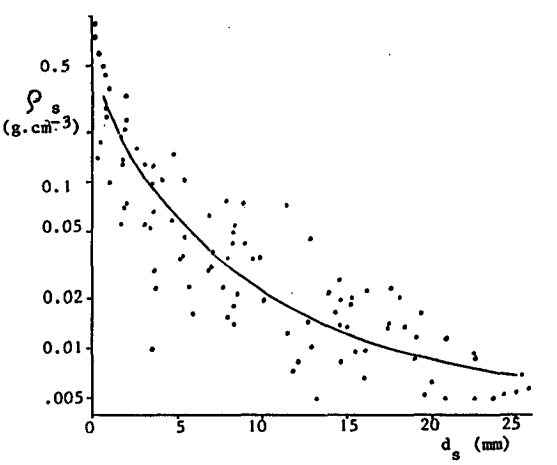

FIG. 1. Simulated density vs snowflake size. Closed circles show the results from the random distribution; the curve shows average results.

(dry snow) to 1 (hail). In the model, e is taken as a fitting parameter. For $e = 0.2$ a good representation of the measurements of Locatelli and Hobbs (1974) on lump graupel is found.

For melting particles we assume that the volume of the particle is proportional to the melted fraction until the particle is saturated with water. The resulting density ρ_f is given by

$$\rho_f = \rho_e/(1 - f). \tag{9}$$

After saturation the density is linearly interpolated between the densities of ice and water.

e. Fall velocity

The terminal fall velocity V of the particles is calculated from the drag resistance R_d by

$$R_d = 0.5 C_d A \rho_a V^2$$

$$R_d = mg$$

so

$$V^2 = \frac{4 d_f \rho_f g}{3 \rho_a C_d}, \tag{10}$$

where

C_d the (nondimensional) drag coefficient
A the horizontal cross section, $A = \pi/4 d_f^2$
g the acceleration due to gravity, taken as $g = 9.81$ m s^{-1}
ρ_a the density of the surrounding air
d_f the diameter of the melting particle.

The drag coefficient depends on the shape of the particle. For rain drops $C_d \approx 0.5$; for hail $C_d \approx 0.5$ (List et al. 1973); for soft hail (Knight and Heymsfield 1983) and graupel (List and Schemenauer 1971) $C_d \approx 0.8$. For snow Magano and Nakamura (1965) take $C_d = 1.3$, but an inspection of their measurements shows $C_d = 1.0$, with some decrease for the lowest densities. Matsuo and Sasyo (1981a) find the drag coefficient of snowflakes ranging from 0.6 to 1.2. It seems that the observations can be represented well by

$$C_d = 1.0 - 0.5e \tag{11}$$

For $e = 0$ a good agreement with the mean results of Langleben (1954) (see Fig. 2) is obtained and the scatter in the results is in good agreement with the observations by Locatelli and Hobbs (1974). Equation (11) is used until the particle is saturated with water. After saturation the fall velocity is linearly interpolated to the value for raindrops, given by Atlas et al. (1973):

$$V = 9.65 - 10.3 \exp(-0.6 d_w) \tag{12}$$

where V is given in m s^{-1} and d_w in mm. Finally, the fall velocity is corrected for air density according to Beard (1985).

The drag coefficient C_d is compared to the heat exchange coefficient C_h. For spheres $C_h = 1$, and the only

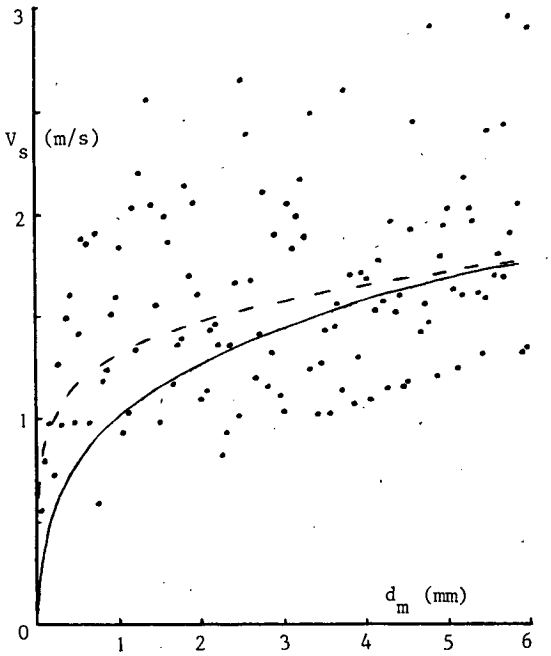

FIG. 2. Simulated fall velocity of snowflakes vs melted size. Closed circles show results from the random distribution, the dashed curve shows the average result; and the solid curve shows the result of Langleben (1954).

measurement for snow (Matsuo and Sasyo 1981a) gives $C_h = 1.75$, independent of the melted fraction. For other ice particles, measurements of C_h are not available. Both exchange factors depend on the particle shape and the flow around the particle, but only C_d depends on air pressure gradients around the particle. In the model the measurements are represented by

$$C_h = 2C_d = 2 - e. \tag{13}$$

f. Reflectivity

The reflectivity of the melting particles is calculated from the Mie scattering matrix for spherical particles using an average dielectric constant ϵ_{av} of the ice–water–air mixture. The dielectric constant is calculated in two steps: first, the average dielectric constant of the ice–water mixture is determined and then that of the wet ice–air mixture.

The average dielectric constant of the ice-water mixture is calculated from the Maxwell–Garnet theory for ice inclusions in a water matrix. This theory is extended by Bohren and Battan (1982) to elliptical inclusions, giving

$$\epsilon_{av} = \frac{(1 - f_v)\epsilon_m + f_v \beta}{1 - f_v + f_v \beta}, \tag{14}$$

$$\beta = \frac{2\epsilon_m}{\epsilon - \epsilon_m} \left\{ \frac{\epsilon}{\epsilon - \epsilon_m} \mathrm{Clog}(\epsilon/\epsilon_m) - 1 \right\},$$

where ϵ_{av} is the dielectric constant of the mixture, ϵ_m the dielectric constant of the matrix, ϵ the dielectric

constant of the inclusions, and f_v the volume fraction of the inclusions. Clog is the complex logarithm.

In the first step, one may clearly use ice as inclusion and water as matrix while the melted water surrounds the ice crystals (Knight 1979; Fujiyoshi 1986). Ice inclusions in a water matrix give the best agreement with the observed reflectivity of melting hail (Bohren and Battan 1982).

With respect to the second step, we have only laboratory observations by Cumming (1952) for dry snowflakes or observations on snow cover (Colbeck 1982; Hallikainen et al. 1986). For dry snow all the models for determining the average dielectric constant give an acceptable agreement with the observations, but for melting snow the results deviate strongly as illustrated in Fig. (3). The reflectivity excess Z_x is defined as

$$Z_x = Z_m/Z_r, \tag{15}$$

where Z_m is the reflectivity during melting, and Z_r the reflectivity of the resulting rain after melting.

Figure 3 is calculated using the Rayleigh approximation, valid when the reflectivity is not influenced by electro-magnetic resonances. Then

$$Z_x = K_m^2/K_r^2 = \left[\frac{(\epsilon_{av} - 1)(\epsilon_w + 2)}{(\epsilon_{av} + 2)(\epsilon_w - 1)}\right]^2, \tag{16}$$

where ϵ_w is the dielectric constant of water.

The following models were used in Fig. (3):

1) The homogeneous mixture ascribed to Debye (1929) is intended for substances with elements too small for a bulk dielectric constant, such as molecules. All other models are intended for mixtures with larger elements.

2) The effective medium model (Bruggeman 1935), is set up for mixtures where all elements are individual.

3) The matrix model (Maxwell Garnet 1904), is one where we find individual elements of one substance in a matrix of interconnected elements of the other substance.

The dielectric constant of two concentric spheres was determined by Aden and Kerker (1951); it is frequently used for melting snow with water as the outer sphere.

Figure 3 is calculated assuming a dry snow density of 0.01 g cm^{-3}, which increases during melting to the value of water according to (9). The figure is compared to Fig. 1 of Battan and Bohren (1982), where a density of pure ice was used. The reflectivity excess for the homogeneous mixture and effective medium models appears to be almost independent of the dry snow density, while for the matrix and concentric sphere models the Rayleigh reflectivity during melting is almost inversely proportional to the dry snow density. Note that the matrix model gives a slight increase in the reflectivity of dry snow, compared with the other models.

The matrix model is used in Fig. 3 by taking wet ice as the matrix. At first glance one might take air as the matrix because of its high volume fraction. However, the matrix model is intended for all volume fractions and this argument has to be set aside. The reflectivity and attenuation are caused by the (wet) ice and not by the air, so the structure of the wet ice is particularly

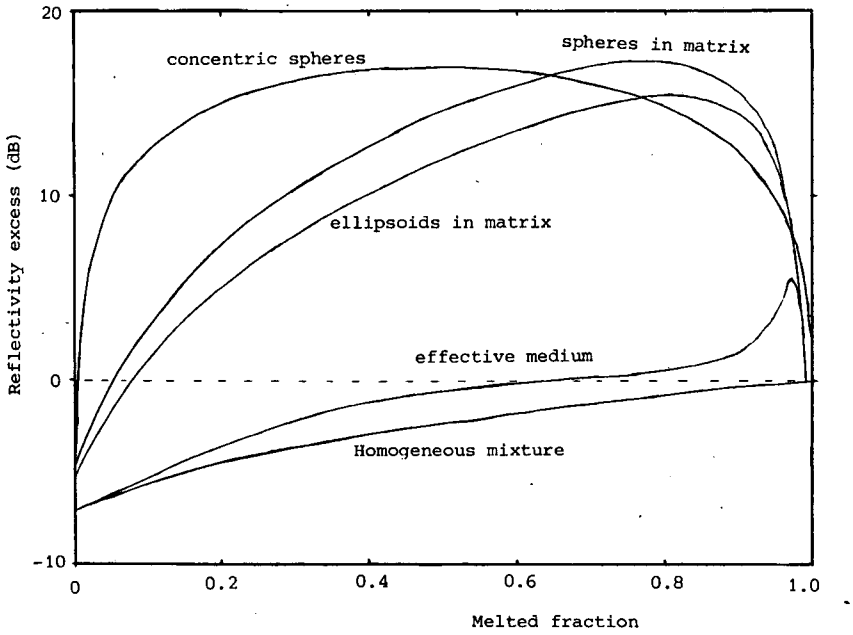

FIG. 3. Reflectivity during melting at 3.3 GHz in the Rayleigh approximation for a spherical snowflake of 0.01 g cm^{-3} initial density as calculated with various models discussed in the text.

important. For separated ice crystals the air should be taken as matrix, but for interconnected ice crystals it is more obvious to take the crystals as matrix. According to Fujiyoshi (1986) the model of air holes in a wet ice frame is characteristic for the middle stage of melting. In the first stage, individual water droplets are formed at the tips of the crystals and in the final stage a lenslike particle is formed. A sudden transition between isolated inclusions and continuous liquid water over the pore space is also observed during the melting of snow cover. For simplicity we will use the model of elliptical air holes in an ice matrix for all stages of melting.

g. *Calculation method*

The following variables have to be determined in the model: 1) air pressure at the onset of melting p_0; 2) precipitation intensity at the onset of melting R_0; 3) median melted particle size d_0; 4) empirical ice density factor e; and 5) the vertical air velocity V_a.

The air pressure is estimated from the meteorological soundings at de Bilt and the observed height of the melting layer. The other parameters are not observed directly and the values of these parameters are varied until good agreement with the radar observations is found.

The following parameters are derived from the radar observations (see Fig. 4): 1) reflectivity in the rain just after melting Z_r, 2) maximum reflectivity excess during melting Z_{xm}, 3) mean Doppler velocity just before melting V_{d0}, 4) mean Doppler velocity just after melting V_{dr} and 5) bright band–width B, the height interval of increased reflectivity.

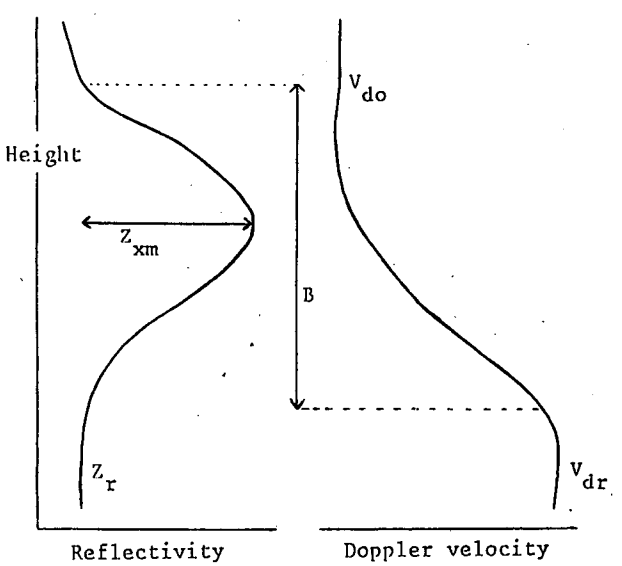

FIG. 4. Schematic profiles of reflectivity and Doppler velocity in the melting layer, showing the input parameters of the simulation model.

The parameters just before and after melting are determined at the boundaries of the bright band. The boundaries of the bright band and thus the bright band–width are determined as follows. Two methods are available for estimating the upper boundary: The first fixes the boundary at the place, where the reflectivity is dropped to the value of the underlying rain; the second uses the first height above the height of maximum reflectivity where $d^2Z/dh^2 > 0$. Generally, with smooth profiles both methods agree within 100 m. In this case the average is used as the upper boundary of the bright band. With larger discrepancies between both methods, the boundary is estimated manually by taking into account the time profile.

The lower boundary is estimated from the Doppler velocity profile. In this way different quantities are used for the detection of the boundaries and a check on consistency can be made. The lower boundary is fixed at the height where the Doppler velocity reaches its maximum value minus 0.5 m s^{-1}. In convective situations corrections are used for vertical variations of mean dropsize and vertical air velocity that mask the velocity maximum. The reflectivity and Doppler velocity just after melting, Z_r and V_{dr}, are determined 100 m below the lower boundary of the bright band.

As shown in section 3, the five radar-derived parameters are not completely independent. The radar-derived parameters at the bright band boundaries hardly change systematically with height outside these boundaries. As a result these input parameters are almost unaffected by the choice of these boundaries. The dependence between the radar-derived parameters is believed to be caused by correlations between the input parameters, for instance between R_0 and d_0. By treating the radar-derived parameters as independent in the calculations, correlations in the observations will return in the input parameters.

Four of the radar-derived parameters are used to determine the input parameters of the model by a fitting procedure, while the fifth is used for verification. The fitting procedure appears to be most convergent when V_{d0} is taken as a verification parameter, when a fit is found after four to eight tries. As a first step the input parameters are set at

$$R_0 = (Z_r/200)^{1/1.6} \quad [\text{mm h}^{-1}]$$

$$d_0 = 5.67/4.1R^{0.21} \quad [\text{mm}]$$

$$V_a = 0.3 \quad [\text{m s}^{-1}]$$

$$e = 0.3.$$

Then the parameters are varied empirically, keeping in mind that Z_{xm} is mainly determined by e; B by R/V_a, $V_{dr} - V_a$ by d_0, and Z_r/R by d_0. The input parameters are varied until the reflectivities are simulated within 0.1 dB, the velocity within 0.05 m s^{-1} and the bright-band width within 5%. The fitting procedure takes almost one hour of calculation time on an

HP1000-A900 minicomputer. The results are presented statistically.

The model gives a solution for an upward and a downward vertical air velocity, as the lapse rate in (3) is determined by the absolute value of V_a. The upward wind results in some condensate production, preferably at the colder melting particles and thus delivering part of the melting heat. With a downward wind the relative humidity of the air is expected to decrease, which results in a start of the melting at a dry bulb temperature above 0°C. Both solutions seem realistic; the upward wind solution may occur most frequently, as precipitation generally results from rising air, but in the decaying stage a downward wind might be more likely. Based on the Doppler velocities observed (see Fig. 7) it was decided to use the upward wind solution only.

In a few transient situations of an extremely bright melting layer, the model was not able to simulate the maximum reflectivity excess Z_{xm}. The simulated Z_{xm} is mainly influenced by the choice of the density parameter e. A correct simulation was possible for $e < 0$, indicating snow of extremely low density. However, an underestimation of Z_{xm} with 1–2 dB at $e = 0$ is preferred while the observed Z_{xm} is influenced by transient and height dependent fluctuations in the precipitation intensity.

3. Measurements

The melting layer is observed with the Delft Atmospheric Research Radar, described by Ligthart and Nieuwkerk (1980). This is a high resolution *FM–CW* radar. The main characteristics are as follows:

Center frequency	3.315 GHz (λ = 9 cm)
Antenna beamwidth	4.6 degrees (receiver) 1.8 degrees (transmitter)
Minimum range of full beam overlap	0.5 km
Range resolution	30 m
Doppler velocity resolution	0.56 m s^{-1} (1983); 0.14 m s^{-1} (1985)
Observation time for complete Doppler spectrum	0.2 s (1983); 0.6 s (1985)

The measurements were performed with the radar scanning vertically. A disadvantage of the *FM–CW* principle is some "cross talk" between succeeding range bins. Range cross talk decreases from −7 dB to the closest neighboring bin to < −20 dB when the range is more than two bins removed. Range cross talk results in some smoothing, but even in the bright band the practical consequences are limited, due to the high range resolution.

The radar observations were made in 1983 and 1985. In 1983 most of the observations were made in slightly convective rainbands (regions of intensified precipitation) within a larger area of stratiform precipitation; in 1985 the observations were made of individual showers of moderate convectivity. In 1983 the melting layer was shown prominently as a bright band in the radar reflectivity pattern, while in the 1985 observations the melting layer was often obscured by convective fluctuations in the precipitation intensity.

Out of the three hours of observation in 1983, a subset of 50 measurements of one minute was selected to represent the full range of reflectivity values observed just below the melting layer. One observation was deleted as it showed two distinct reflectivity maxima around the melting layer. All one minute averages of the 1985 observations are used to characterize the melting layer, but for verification of the stationary model the data showed too much meteorological scatter. Because of the high data repetition frequency of the radar, the one-minute averages are essentially free of quantization noise.

4. Results

a. Observed characteristics of the melting layer

The melting layer characteristics are shown versus the reflectivity in rain just after melting, Z_r, as this parameter gives an indication of the precipitation intensity.

The maximum reflectivity excess Z_{xm} (the maximum reflectivity in the melting layer divided by Z_r) is almost independent of Z_r (Fig. 5) and shows a large scatter. Values between 7 and 15 dB, with an average of 11 dB are found in the slightly convective rainbands. During showers lower values are found; a value of 0 dB means that the reflectivity during melting is always below the value of the resulting rain.

The bright-band width increases from 200 m at Z_r = 20 dB to 600 m at Z_r = 45 dB (Fig. 6) with a scatter of some 100 m. The observations during showers are not included as they show much more scatter, mainly while the boundaries of the bright band are determined with less accuracy. During showers the variations in reflectivity and mean Doppler velocity take about the same height interval as in less convective precipitation, but according to the model the particles may fall several hundreds of meters (to more than 1 km for hail) under the region of varying radar observations, as the fall velocity and refractive index hardly change after the particle is saturated with melted water. The results on maximum reflectivity excess and peak width deviate slightly from the Chilbolton radar results; the latter do not show a dependence of bright-band width on reflectivity, but show an increase of maximum reflectivity excess with increasing reflectivity from Z_{xm} = 5 dB at Z_r = 25 dBZ to 12 dB at 35 dBZ (COST 205, 1985). This deviation might be influenced by the poorer vertical resolution of the Chilbolton radar.

The mean Doppler velocities just before and after melting are shown in Fig. 7 for the rainband obser-

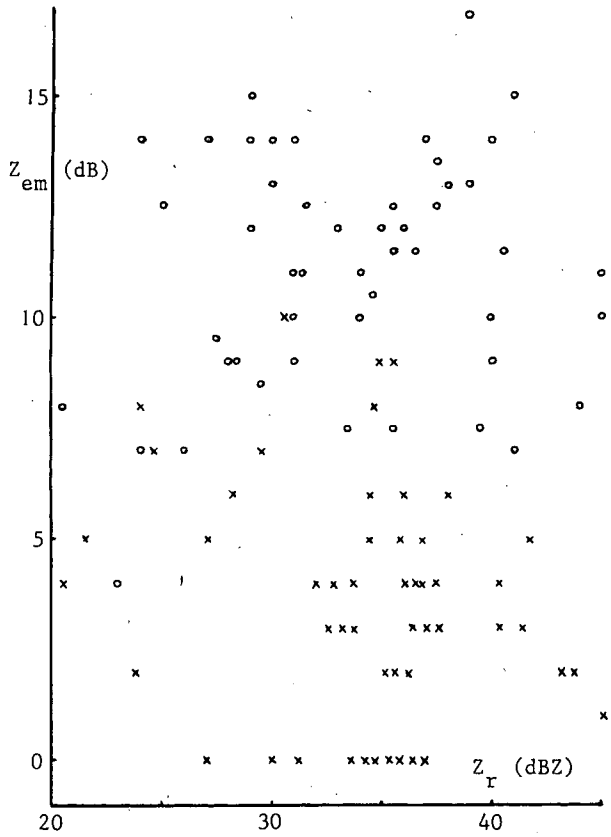

FIG. 5. Maximum reflectivity excess in the melting layer vs reflectivity just below the melting layer: o = observed in the rainbands, 1983; x = observed in the showers, 1985.

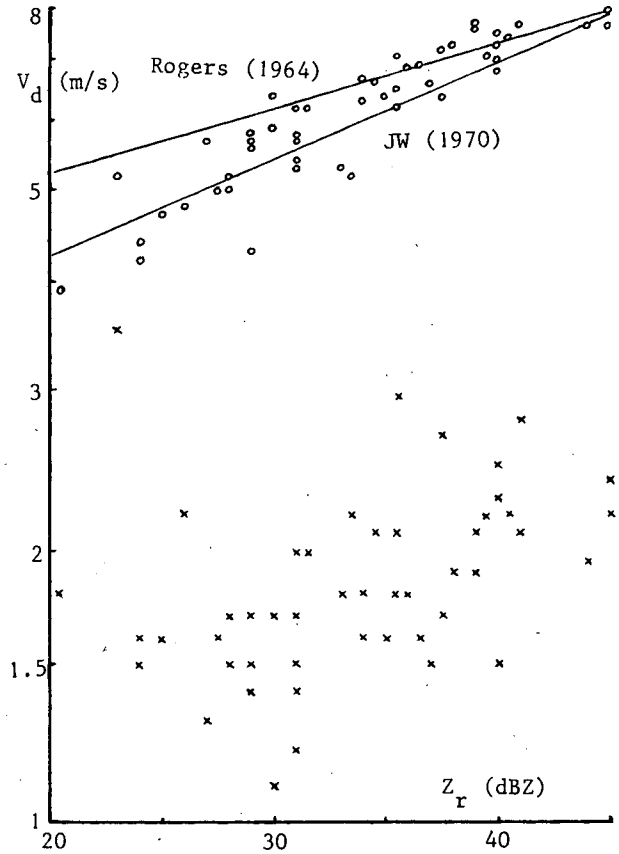

FIG. 7. The mean Doppler velocities just above (x) and below (o) the boundaries of the bright band for the rainband observations. Also shown are the empirical Joss-Waldvogel (JW) (1970) relation and the theoretical Rogers (1964) relation.

vations. The mean Doppler velocity before melting falls around 2 m s^{-1} with a large relative scatter. The mean Doppler velocity just after melting is in good agreement with the empirical Joss and Waldvogel (1970) relation:

$$V_{dr} = 2.6Z^{0.107} \tag{17}$$

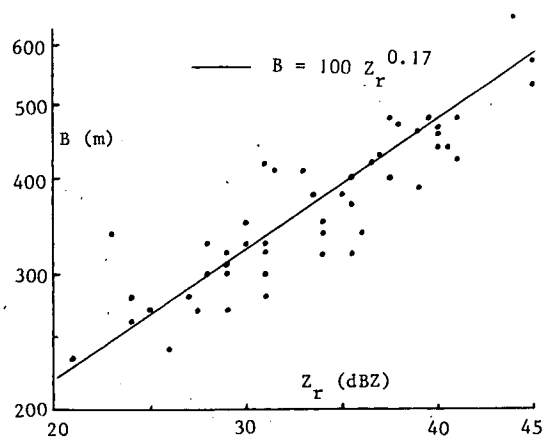

FIG. 6. Width of the bright band vs reflectivity for the rainband observations.

and falls below the Rogers (1964) relation:

$$V_{dr} = 3.8Z^{0.071} \tag{18}$$

The Rogers relation was derived for a Marshall–Palmer drop size distribution with a zero vertical air velocity; a smaller mean Doppler velocity may be caused by 1) an upward vertical air velocity; and 2) a distribution of smaller raindrops. The first motivated upward wind solution for the simulations. The second may also take part during the low reflectivity values observed during the decaying (dissipating) stage of the rain events. In this stage, when the largest deviations from the Rogers relation are found, smaller drops (Carbone and Nelson 1978) seem more likely than high upward velocities.

The mean Doppler velocities during the 1985 showers show more scatter; the values in the ice phase are generally larger and in the rain phase smaller than those encountered in the rainbands. The lower velocities in the rain can be explained by higher vertical air velocities and the higher values in the ice phase by faster falling and denser ice particles.

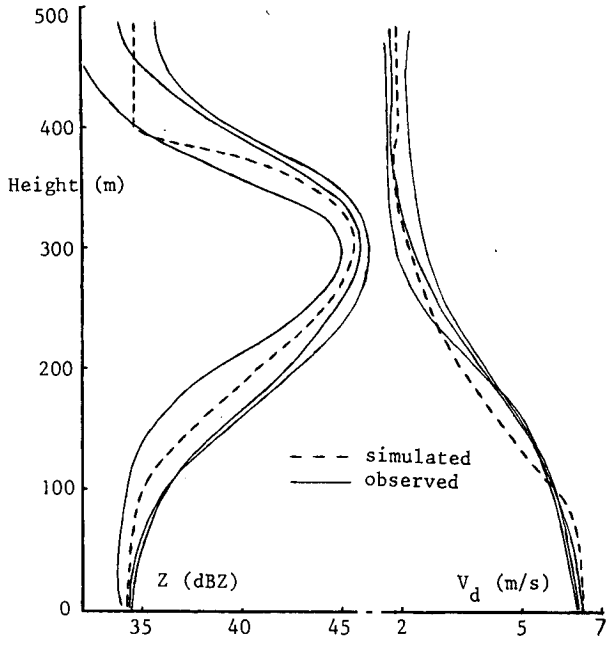

FIG. 8. Vertical profiles of reflectivity and mean Doppler velocity in the melting layer during stratiform precipitation. The observations are averaged over one minute.

b. *Vertical profiles of reflectivity and mean Doppler velocity*

Three profiles observed on different days in 1983 are shown in Fig. 8, together with a simulated profile. The observed profiles were selected on the basis of their reflectivity that is close to the average of all measurements, and their lack of meteorological disturbances. The figure shows that the observed profiles can be simulated accurately. Two minor deviations are found: the change in reflectivity at onset of melting and the change in mean Doppler velocity during the second half of melting. Some smoothing in the observed Doppler velocity profile near the end of melting is caused by range cross talk of the radar: the highest reflectivity in the bright band is found at a velocity that is close to the fall velocity of snow. As a result, the observed Doppler velocity near the end of melting is slightly centered to the fall velocity of snow. The abrupt change in the simulated reflectivity at the onset of melting is more likely to result from the matrix model for calculation of the dielectric constant: in the first stage of melting the melted water is not yet interconnected, resulting in a slower increase of reflectivity than given by the model.

Figure 9 shows simulated profiles of different versions of the model. All versions can simulate an almost identical reflectivity profile, but the simulated mean Doppler velocity during the first half of melting varies. The version with spontaneous breakup gives the most accurate representation of the velocity profile and is used for further simulations. The scatter in the particle density increases the scatter in the distance needed to fall before complete melting, resulting in a closer agreement with the observed velocity profile. The opposite is found for collisional aggregation, as the model uses only one average melted fraction per particle size

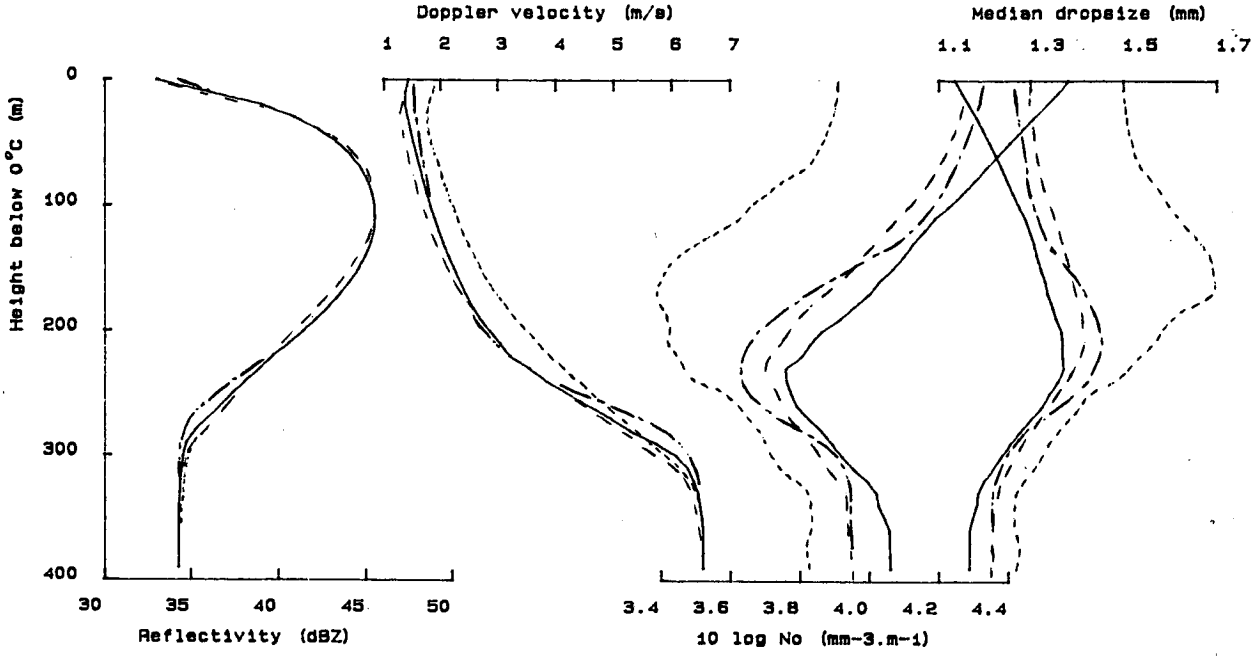

FIG. 9. Simulated profiles of reflectivity and mean Doppler velocity and the particle size distribution parameters in the melting layer using different versions of the model: (long-short dashes) model without variations in ice density; (dashed) basic model; (solid) model with collisional aggregation/breakup; (short dashes) model with spontaneous breakup.

interval. Collisional aggregation appears important above the melting layer, but is restricted within the melting layer where the number of collisions is small, due to the small height interval of this layer.

The median particle size and N_0 as shown in Fig. 9 were calculated from an exponential fit on the particle size distribution between 1 and 4 mm melted diameter, as discussed by Gordon and Marwitz (1984). Even the models without aggregation and breakup show an increase in the median particle size in the melting layer. This is caused by the faster melting of the smaller particles, resulting in a larger fall velocity and a smaller number density. A similar explanation is found for the small decrease of the simulated mean Doppler velocity in the first tens of meters of melting, in spite of the increase in fall velocity for all melting particles: As the slower falling particles melt faster, they show a faster increase in reflectivity and the (reflectivity weighted) mean Doppler velocity decreases.

It appears much more difficult to assess the model input parameters for the 1985 showers. Figure 10 shows that it is even difficult to determine the height of the melting layer from the one-minute data. The melting layer height can be fixed more accurately from the profile that is averaged over the whole shower (especially from the velocity profile). When the model is used to simulate an average profile over the whole shower, the observed rain intensity is overestimated by a factor of 2; when the model is used with the observed rain intensity as input parameter, the bright-band width is much smaller than observed. The large observed width can be explained by fluctuations of the 0°C height during the shower.

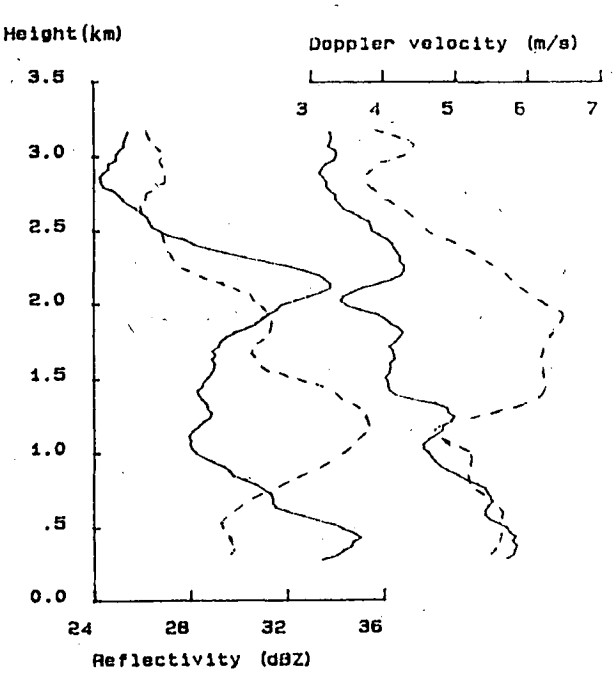

FIG. 10. Vertical profiles of reflectivity and mean Doppler velocity. The profiles are averaged over one minute and observed directly after each other. The melting layer is situated around 2 km in height.

c. Simulated characteristics of the melting layer

As stated earlier, the mean Doppler velocity just before melting (V_{d0}) is used as a verification parameter. It is shown in Fig. 11, illustrating a large scatter without systematic deviations. In Fig. 12 the difference between the simulated and observed V_{d0} is shown versus Z_r. Again we find a good overall agreement; the scatter appears to increase with Z_r. The scatter can be caused by errors in the simulated fall velocity or vertical air velocity. Given the small fall velocities of the ice particles (mostly below 2 m s^{-1}) it is unlikely that the scatter in V_{d0} would be caused by errors in the fall velocity. Scattered errors in the vertical air velocity are more likely: the vertical air velocity is primarily used in the model to determine the bright-band width, as V_a and R determine the extension of the (almost) isothermal layer in the upper part of the melting layer. As the temperature adapts slowly to variations in V_a and R, the model finds some average vertical air velocity and cannot account for the actual fluctuations.

The simulated vertical air velocity is shown in Fig. 13 for the rainband situations. The simulated V_a increases with reflectivity, which is acceptable as stronger upward winds are needed to form higher rain intensities. The small scatter in V_a emphasizes the averaging caused by the assumption of stationarity in the model. During showers upward winds of 2 m s^{-1} were simulated, so the model is capable of simulating vertical air velocities which deviate sharply from the values listed in Fig. 13. Given the good overall agreement of V_{d0} it is expected that the vertical air velocity will be simulated without systematic errors, although the actual fluctuations are neglected.

The simulated rain intensity just after melting is tested on meteorological acceptability and shown in Fig. 14. The result falls well within the ranges given by Ulbrich and Atlas (1978), which were determined from 59 Z–R relations as put into table form by Battan (1973). For $Z > 30$ dBZ the simulations are in good agreement with the Marshall–Palmer relation ($Z = 200R^{1.6}$), while for lower reflectivities the simulations fall above that relation. As discussed in relation to Fig. 6 the low reflectivity values were observed during the dissipating stage of the rainbands when we may expect relatively small drops that result in a relatively high rain intensity at a given reflectivity, as compared to the Marshall–Palmer values.

The simulated maximum reflectivity excess Z_{xm} is plotted versus the mean ice density (Fig. 15). The mean ice density is defined as the total ice mass divided by the total volume of all ice particles in a certain air volume just before melting. The scatter of Fig. 15 appears mainly dependent on the median melted particle size of the initial distribution. The simulated mean ice den-

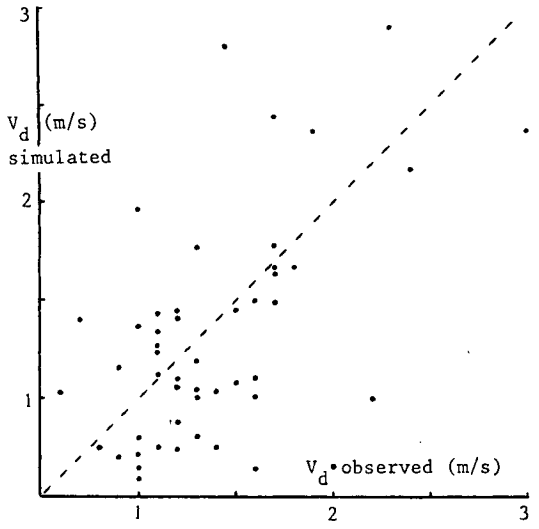

FIG. 11. Simulated vs observed mean Doppler velocity just before melting.

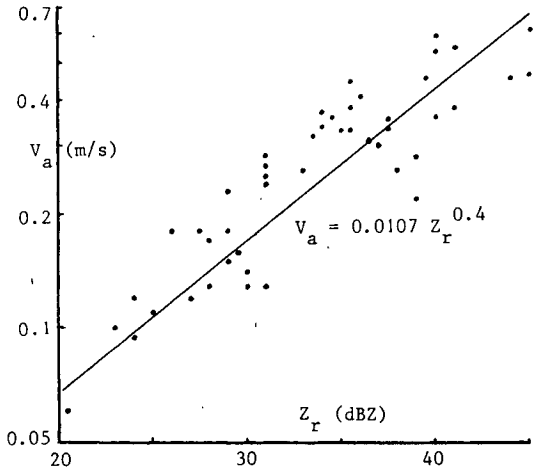

FIG. 13. Simulated vertical air velocity in the melting layer vs reflectivity just after melting for the rainband observations.

sity in the rainbands ranges between the value of pure snow to values an order of 10 higher. In the showers even larger values, those approaching hail, are observed. Figure 15 clearly demonstrates that it is essential to vary the ice density for a realistic simulation of the reflectivity in the melting layer.

5. Conclusions

1) The melting layer often appears as a prominent bright band in the radar observations. Further, it was found that the existence of a bright band is related to the density of the ice particles, rather than to the rain intensity.

2) The width of the bright band increases with rain intensity. According to our model, this is mainly caused by a wider (almost) isothermal layer at the upper part of the melting layer. At higher ice densities the prominence of the bright band decreases and the melting may proceed up to heights more than 1 km below the band, where radar variations related to melting are observed.

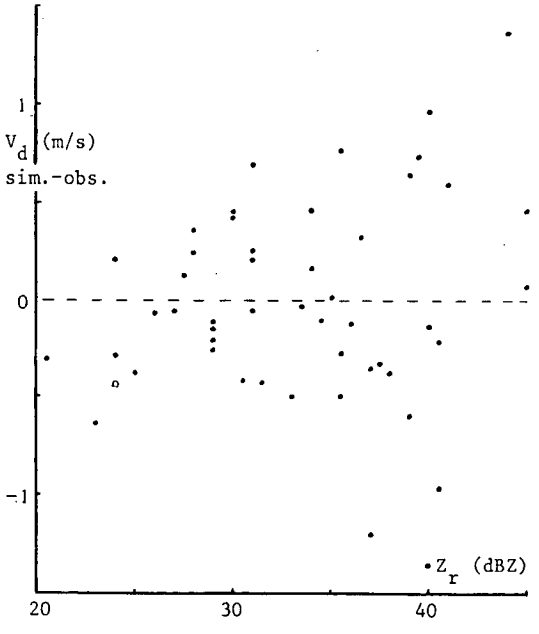

FIG. 12. The difference between the simulated and observed mean Doppler velocity just before melting vs the reflectivity just after melting.

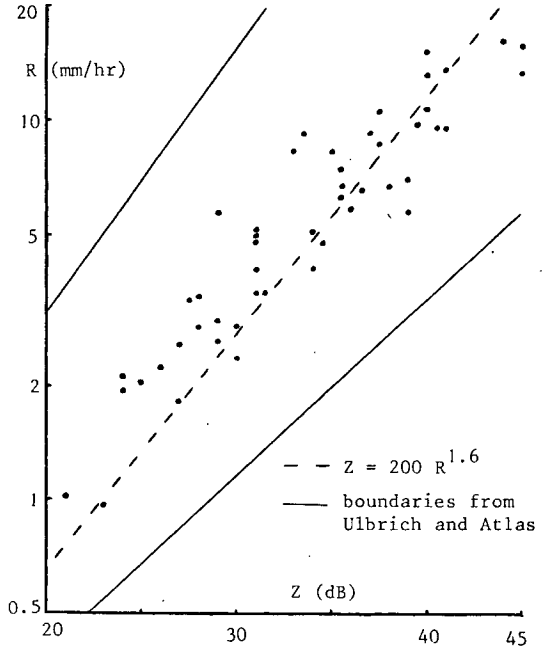

FIG. 14. Simulated rain intensity vs observed reflectivity just after melting. Shown as well are the Marshall–Palmer relation and the ranges of Ulbrich and Atlas.

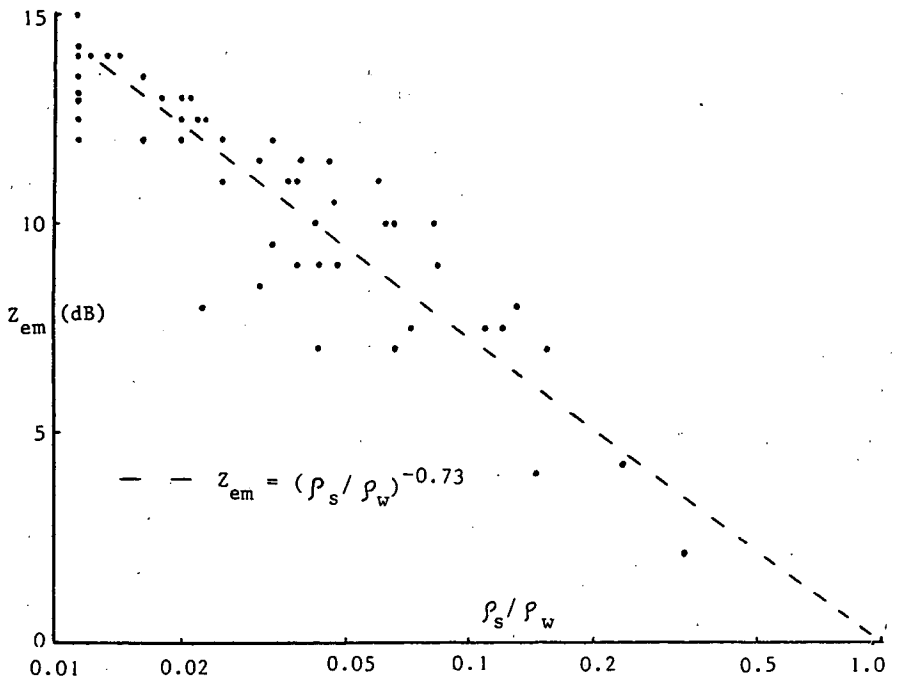

FIG. 15. Observed maximum reflectivity excess in the melting layer vs simulated mean ice density just before melting.

3) The radar reflectivity and mean Doppler velocity can be simulated accurately with the melting layer model in stratiform and slightly convective precipitation. In strong convective situations the observations show too many meteorological fluctuations, which cannot be simulated by a stationary model.

4) Several new methods have been adapted successfully in the model: The average dielectric constant of melting particles could be calculated well from the theory of inclusions in a matrix when the air is taken as inclusions within the melting ice frame. It appeared essential to fit the ice density between the values of snow and hail for a realistic simulation of the reflectivity in the melting layer. Including variations around the mean ice density and spontaneous breakup near the end of the melting improved the simulation, but it appeared not to be useful to include collisional aggregation/breakup. Apparently, calculation of the temperature profile in the melting layer is essential in order to simulate the observed width of the bright band, although the resulting vertical air velocity is an averaged value that does not account for actual fluctuations.

Acknowledgments. The study was supported by the Netherlands Technology Foundation (STW) under Grant DEL25.0359 and initiated by L. P. Ligthart. The melting layer model was discussed with A. W. Dissanayake (ESA) and H. R. A. Wessels (KNMI). The Mie scattering algorithm was provided by H. W. J. Russchenberg. The radar was operated by J. H. Zijderveld and the data transmission was provided by J. S. van Sinttruyen and L. R. Nieuwkerk. Meteorological instruments were placed at our disposal by the Physisch Lab. TNO, Waalsdorpervlakte at TNO Zuidpolder and operated by P. Hoogeboom and J. Kleyweg. The text was corrected by S. Massotty and J. B. Zaat-Jones.

REFERENCES

Aden, A. L., and M. Kerker, 1951: Scattering of electromagnetic waves by two concentric spheres. *J. Appl. Phys.*, **22**, 1242–1246.

Atlas, D., R. C. Srivastava and R. S. Sekhon, 1973: Doppler radar characteristics of precipitation at vertical incidence. *Rev. Geophys. Space Phys.*, **2**, 1–35.

——, R. Tatehira, R. Srivastava, W. Marker and R. Carbone, 1969: Precipitation induced mesoscale wind perturbations in the melting layer. *Quart. J. Roy. Meteor. Soc.*, **95**, 544–560.

Austin, P. M., and A. Bemis, 1950: A quantitative study of the bright band in radar precipitation echoes. *J. Meteor.*, **7**, 165–171.

Battan, L. J., 1973: *Radar Observation of the Atmosphere*, University of Chicago Press, 279 pp.

——, and C. F. Bohren, 1982: Radar backscatter by melting snowflakes. *J. Appl. Meteor.*, **21**, 1937–38.

Beard, K. V., 1985: Simple altitude adjustments to raindrop velocities for Doppler radar analysis. *J. Atmos. Oceanic Technol.*, **2**, 468–471.

Bohren, C. F., and L. J. Battan, 1982: Radar backscatter by spongy ice spheres. *J. Atmos. Sci.*, **39**, 2623–29.

Brazier-Smith, P. R., S. G. Jennings and J. Latham, 1973: Raindrop interactions and rainfall rates within clouds. *Quart. J. Roy. Meteor. Soc.*, **99**, 260–272.

Bruggeman, D. A. G., 1935: Berechnung verschiedener physikalischer Konstanten von heterogenen Substanzen. *Ann. Phys. (Leipzig)*, **24**, 636–679.

Carbone, R. E., and L. D. Nelson, 1978: The evolution of raindrop spectra in warm based convective storms as observed and numerically modelled. *J. Atmos. Sci.*, **35**, 2303–14.

Colbeck, S. C., 1982: The geometry and permittivity of snow at high frequencies. *J. Appl. Phys.*, **53**, 4495–4500.

COST 205, 1985: Project COST 205: Precipitation studies. *Alta Freq.*, **54-3**, 116–132.

Cumming, W. A., 1952: The dielectric properties of ice and snow at 3.2 cm. *J. Appl. Phys.*, **23**, 768.

Debye, P., 1929: Polar Molecules, the Chemical Catalog Company, 172 pp.

Dissanayake, A. W., and N. J. McEwan, 1978: Radar and attenuation properties of rain and bright band. IEE Conf. Publ. 169-2, 125–129.

Fujiyoshi, Y., 1986: Melting snowflakes. *J. Atmos. Sci.*, **43**, 307–311.

Gordon, G., and J. D. Marwitz, 1984: An airborne comparison of three PMS probes. *J. Atmos. Oceanic Technol.*, **1**, 22–27.

Hallikainen, M. T., F. T. Ulaby and M. Abdelrazik, 1986: Dielectric properties of snow in the 3–37 GHz range. *IEEE Trans. Antennas Propagat.*, **AP-34**, 11, 1329–1339.

Hobbs, P. V., S. Chang and J. D. Locatelli, 1974: The dimensions and aggregations of ice crystals in natural clouds. *J. Geophys. Res.*, **79**, 2199–2206.

Joss, J., and A. Waldvogel, 1970: Raindrop size distributions and Doppler velocities. *Preprints, 14th Radar Meteorology Conf.*, Boston, Amer. Meteor. Soc., 153–156.

Knight, C. A., 1979: Observations of the morphology of melting snow. *J. Atmos. Sci.*, **36**, 1123–29.

Knight, N. C., and A. J. Heymsfield, 1983: Measurement and interpretation of hailstone density and terminal velocity. *J. Atmos. Sci.*, **40**, 1510–16.

Langleben, M. P., 1954: The terminal velocity of snowflakes. *Quart. J. Roy. Meteor. Soc.*, **80**, 174–181.

Leitao, M. J., and P. A. Watson, 1986: Method for prediction of attenuation on earth-space links based on radar measurements of the physical structure of rainfall. *IEE Proc.*, **133**, 429–440.

Lhermitte, R. M., and D. Atlas, 1963: Doppler fall speed and particle growth in stratiform precipitation. *Proc. 10th Radar Weather Conf.*, 297–302.

Ligthart, L. P., and L. R. Nieuwkerk, 1980: *FM-CW* Delft Atmospheric Research Radar. *IEE Proc.*, **127-F**, 421–426.

List, R., and R. S. Schemenauer, 1971: Free fall behaviour of planar snow crystals, conical graupel and small hail. *J. Atmos. Sci.*, **28**, 110–115.

——, U. W. Rentsch, A. C. Byram and E. P. Lozowski, 1973: On the aerodynamics of spheroidal hailstone models. *J. Atmos. Sci.*, **30**, 653–661.

——, and J. R. Gillespie, 1976: Evolution of raindrop spectra with collision induced breakup. *J. Atmos. Sci.*, **33**, 2007–13.

Locatelli, J. D., and P. V. Hobbs, 1974: Fall speeds and masses of solid precipitation particles. *J. Geophys. Res.*, **79**, 2185–98.

Magano, C., and T. Nakamura, 1965: Aerodynamic studies of falling snowflakes. *J. Meteor. Soc. Japan*, **43**, 139–147.

Matsuo, T., and Y. Sasyo, 1981a: Empirical formula for the melting rate of snowflakes. *J. Meteor. Soc. Japan*, **59**, 1–8.

——, and Y. Sasyo, 1981b: Melting of snowflakes below freezing level in the atmosphere. *J. Meteor. Soc. Japan*, **59**, 10–24.

——, 1984: Melting of snowflakes in the atmosphere. *Proc. 9th Int. Cloud Physics Conf.*, Ac. Sci. Estonian SSR, 279–281.

Maxwell, Garnet, J. C., 1904: Colors in metal glasses and in metallic films. *Phil. Trans. Roy. Soc. London*, **A203**, 385–420.

Nishitsuji, A., M. Hoshiyama, J. Awaka and Y. Furuhama, 1983: An analysis of propagative character at 34.5 GHz and 11.5 GHz between ETS-11 satellite and Kashima station. On the precipitation model of stratus. Trans. (B), *I.E.C.E., Japan, J66-B*, **9**, 1163–70.

Ohtake, R., 1969: Observations of size distributions of hydrometeors through the melting layer. *J. Atmos. Sci.*, **26**, 545–557.

Passarelli, R. E., and R. C. Srivastava, 1979: A new aspect of snowflake aggregation theory. *J. Atmos. Sci.*, **36**, 484–493.

Rasmussen, R. M., V. Levizzani and H. R. Pruppacher, 1984: A wind tunnel and theoretical study on the melting behaviour of atmospheric ice particles: III. Experiment and theory for spherical ice particles of radius > 500 μm. *J. Atmos. Sci.*, **41**, 381–388.

Rogers, R. R., 1964: An extension of the *Z–R* relationship for Doppler radar. *Proc. 11th Weather Radar Conf.*, Boulder, Amer. Meteor. Soc., 158–169.

Sasyo, Y., and T. Matsuo, 1985: Effects of the variations of falling velocities of snowflakes on their aggregation. *J. Meteor. Soc. Japan*, **63**, 249–261.

Smith, C. J., 1986: The reduction of errors caused by bright bands in quantitative rainfall measurements made using radar. *J. Atmos. Oceanic Technol.*, **3**, 129–141.

Stewart, R. E., J. D. Marwitz, J. C. Pace and R. E. Carbone, 1984: Characteristics through the melting layer of stratiform clouds. *J. Atmos. Sci.*, **22**, 3227–37.

Wexler, R., J. R. Reed and J. Honig, 1954: Atmospheric cooling by melting snow. *Bull. Amer. Meteor. Soc.*, **35**, 48–51.

Ulbrich, C. W., and D. Atlas, 1978: The rain parameter diagram: methods and applications. *J. Geophys. Res.*, **83**, 1319–25.

Yokoyama, T., H. Tanaka, K. Nakamura and J. Awaka, 1984: Microphysical processes of melting snowflakes detected by two wavelength radar. Part II. Application of two wavelength radar technique. *J. Meteor. Soc. Japan*, **62**, 668–677.

——, H. Tanaka, K. Akaeda, T. Ohtani, N. Yoshizawa, M. D. Yamanaka, A. Mita, Y. Ishizaka and A. Ono, 1985: Observations on microphysical processes in the stratiform precipitations including melting layers at Mt. Fuji. *J. Meteor. Soc. Japan*, **63**, 100–111.